The Role of Catalyst Synthesis on the Enhancement of Ni/Pr_2O_3 for the Conversion of Greenhouse Gases to Syngas.

Osarieme Uyi Osazuwa [1, 4], Sumaiya Zainal Abidin [1, 3*], Nurul Asmawati Roslan[2], Xiaolei Fan [5], Herma Dina Setiabudi [1, 2], Dai-Viet N. Vo[6,7], Jude A. Onwudili[8]

[1] *Centre for Research in Advanced Fluid & Processes (FLUID CENTRE), Universiti Malaysia Pahang, 26300 Gambang, Kuantan, Pahang, Malaysia.*

[2]*Faculty of Chemical and Process Engineering Technology, College of Engineering Technology, Universiti Malaysia Pahang, Lebuhraya Tun Razak, 26300 Gambang, Kuantan, Pahang, Malaysia*

[3]*Faculty of Chemical Engineering, Industrial University of Ho Chi Minh City, 12 Nguyen Van Bao St, Go Vap District, Ho Chi Minh City, Vietnam*

[4]*Department of Chemical Engineering, University of Benin, PMB 1154, Benin City Edo State, Nigeria*

[5]*Department of Chemical Engineering and Analytical Science, School of Engineering, The University of Manchester, Oxford Road, Manchester, United Kingdom*

[6]*School of Chemical Engineering, Universiti Sains Malaysia, Engineering Campus, 14300, Nibong Tebal, Penang, Malaysia*

[7]*Institute of Environmental Technology and Sustainable Development, Nguyen Tat Thanh University, Ho Chi Minh City, 755414, Viet Nam*

[8]*Energy and Bioproducts Research Institute, School of Infrastructure & Sustainable Engineering, College of Engineering and Physical Sciences, Aston University, Birmingham B4 7ET, UK*

** Corresponding Author E-mail: sumaiya@ump.edu.my*

Tel: +6094316271

Abstract

Catalytic methane (CH_4) dry reforming (MDR) reaction proceeds with the formation of carbon; hence the effects of the catalyst preparation method on the type of carbon are worth investigating. This study investigates the performance of 20 wt.% Ni/Pr_2O_3 catalysts prepared by incipient wetness impregnation (IWI), ultrasonic wet impregnation (US-WI), and Pechini sol-gel (PSG) methods. The catalyst's crystallite size was approximately 21.3 nm, 21.3 nm, and 10.6 nm, for IWI, US-WI, and PSG catalysts respectively. Temperature effects study showed higher temperature favored the MDR reaction with the side reaction playing vital roles. The catalyst synthesized by the PSG method had higher carbon gasification rate with stability up to 24 h, whereas catalysts from other synthesis methods were only active below 2 h. This can be linked to the higher amount of filamentous carbon formed, balance in oxygen species, and the smaller crystallite size of the PSG-20 wt.% Ni/Pr_2O_3. The PSG-20 wt% Ni/Pr_2O_3 catalyst accumulated more filamentous carbon than graphitic carbon. In contrast, the IWI and US-WI catalysts accumulated mainly graphitic carbon which encapsulated the Ni^0 sites, resulting in excess carbon deposition and reactor clogging within 2 h of reaction time.

Keywords: *Methane dry reforming; greenhouse gases; Nickel catalyst; synthesis method; carbon species; Oxygen species.*

1. Introduction

The increase in the anthropogenic greenhouse gases, which causes global warming has led to researchers developing different techniques to utilize these environmental pollutant gases (CH_4 and CO_2) by reforming them

into more useful feedstock of gaseous fuels or products from gaseous fuels. Therefore, the development of the CH_4 dry reforming (MDR) reaction is an advantageous process technique to mitigate CH_4 and CO_2 and produce synthetic gas which is suitable for Fischer Tropsch Synthesis (Botes et al. 2013; Chen et al. 2020; Khademi et al. 2021). Other researchers have employed MDR reaction to enhance the quality of Anaerobic Digestion (AD) biogas which is mainly composed of CH_4 and CO_2 (Kwon et al. 2018)(Moogi et al. 2022). The product of MDR; synthesis gas (syngas) is utilized as feedstock by several manufacturing processes, hence, making the process vital for various prospective applications (Sun et al. 2022). MDR reaction is highly endothermic in nature; therefore, high temperature which corroborates to high heat energy usage is desired (Li et al. 2020). An alternative to the high energy demand of MDR reaction is the use of highly efficient catalysts which increases the syngas yield (Cao et al. 2022), (Pizzolitto et al. 2019). Because higher yield translates to commercial benefits from the process, it is important to upgrade the catalyst's quality. Some researchers have focused on using noble metal-based catalyst (Rezaei et al. used Ru, Rh, Ir, Pt, Whang et al. used Ru, and Ballesteros-Plata et al. used Pd, Pd-Nb) due to their performance and resistivity towards carbon deposition (Rezaei et al. 2006; Whang et al. 2017; Ballesteros-Plata et al. 2022). Others have used transition metals (Fan et al. used Ni-Co, Baudouin et al. used Ni, Osazuwa et al. used Co) because noble metals are quite expensive (Fan et al. 2011; Baudouin et al. 2013; Osazuwa et al. 2017).
In the current research field, Ni is readily utilized for MDR because it is less expensive and exhibits good performance. Nonetheless, Ni loses its activity easily due to its affinity for carbon deposited during CH_4 cracking (Han et al. 2021; Ekeoma et al. 2022; Kwon et al. 2022). Moreover, excess Ni affects the Ni-support interaction because it minimizes the catalyst's basic strength (Zanganeh et al. 2013). To solve this problem, researchers have focused on designing new catalysts to enhance the MDR reaction (Liu et al. 2012). In developing a new catalyst, one key parameter that significantly affects the catalyst physicochemical properties and performance towards the MDR reaction is the method of catalyst synthesis (Osazuwa et al. 2021). This parameter could potentially minimize catalyst deactivation resulting from carbon deposits, thereby enhancing the catalyst stability.
According to literature, nature of supports and methods of catalysts' synthesis can promote good performance of Ni-based catalysts (Mustu et al. 2015). For instance, alumina (Al_2O_3) in combination with transition metals (Ni, Co) which are widely utilized catalysts in MDR reactions due to their relatively cheap cost and acceptable performance (Schwengber et al. 2016; Franz et al. 2021; Kwon et al. 2022) have been reported to exhibit some deficiencies as support during the synthesis/catalytic process. Common challenges with alumina as supports are alumina dissolution in the aqueous media during supported catalyst synthesis (more evident in Co based catalyst), rehydration of γ-Al_2O_3 during catalyst implementation and thermal degradation (Trueba and Trasatti 2005), (Kim et al. 2004). Silica (SiO_2) in combination with transition metals have been widely utilized and reported (Li et al. 2021; Owgi et al. 2022; Ekeoma et al. 2022) with its major setback being the formation of aggregates/agglomerates during synthesis and its low compatibility with other catalytic materials (Ali et al. 2014), (Mora-Barrantes et al. 2011). Rare earth metal oxides such as Sm, Ce and La possess catalytic properties that make them very effective catalyst supports (Osazuwa and Abidin 2020), (Fang et al. 2018). The step i.e., introducing a rare earth metal as support into the catalyst can limit the carbon formation on the catalyst surface. Moreover, it has been established that rare earth metals oxides (such as cerium (VI) oxide (CeO_2) used by Luisetto et al. and Odedairo et al., Neodymium (III) oxide (Nd_2O_3) used by Ayodele et al., and Praseodymium (III) oxide (Pr_2O_3) used by Ayodele et al.,) can supply oxygen to the reaction media (Luisetto et al. 2012; Odedairo et al. 2013; Ayodele et al. 2016, 2017). Also, the catalyst reducibility and inhibition of carbon formation are some of other benefits of the addition

of alkaline rare earth metals such as Pr to a metallic catalyst (Li et al. 2011). Therefore, expectations are that Pr_2O_3 can improve the basicity of the catalyst while enhancing CO_2 adsorption.

Furthermore, synthesis methods are vital for the overall properties and behavior of the formulated catalysts (Yosefi et al. 2015). For instance, the sol-gel method has been applied to prepare supported catalytic materials (Gonzalez et al. 1997; Sajjadi et al. 2015). Compared to the conventional impregnation technique, the sol-gel technique aids better distribution, thermal resistivity, clogging, and product selectivity (Gonçalves et al. 2006). However, its effect on the formation of specific carbon types and the adsorbed/lattice oxygen of the catalyst have rarely been mentioned in literature.

In this study, the influence of synthesis methods on the physical/chemical properties and performance of the Ni/Pr_2O_3 catalyst for MDR reaction was established. The novelty of this present study pertains to the investigation, determination, and comparison of the behavior of the 20 wt.% Ni/Pr_2O_3 catalyst from three different preparation methods (incipient wetness impregnation (IWI), ultrasonic wet impregnation (US-WI), and Pechini sol-gel (PSG) methods) to ascertain the role of the synthesis method. Also, the types of carbon species formed during the reactions were also identified and the oxygen species associated with each catalyst was related to the carbon gasification and catalyst performance during the MDR reaction. Several characterizations were carried out on all the catalysts to ascertain their physicochemical properties and how these properties affect the MDR reaction at the selected 20 wt.% Ni catalyst loading. In addition, the relationship between catalyst preparation and the performance of the 20 wt.% Ni/Pr_2O_3 catalyst at different reaction temperatures was also tested to support the conclusion reached after detailed catalyst characterization. Finally, the best synthesis procedure was selected to ascertain the catalyst stability in the MDR reaction.

2. Experimental

2.1. Catalyst Synthesis

In this present study, 20 wt% Ni/Pr_2O_3 was synthesized using three different synthesis methods: the incipient wet impregnation (IWI), ultrasonic-assisted wet impregnation (US-WI) and the Pechini sol-gel (PSG) methods. Nitrate salt of Ni and Pr (99.9%, Sigma Aldrich), citric acid ACS reagent > 99.5% (anhydrous), and ethylene glycol, analytical reagent liquid, 99.8% were employed during the catalysts' preparation. Also, 20 wt.% of Ni was adopted as the ideal amount of Ni required since existing literature have reported this amount as the optimum Ni wt.% loading that can give the desired catalytic behavior in the MDR reaction (Sepehri et al. 2018). In comparison, others have applied 20 wt.% of Ni catalyst for methane reforming (Amin et al. 2012) and butanol reforming, respectively (Varkolu et al. 2021).

2.1.1. Synthesis of the Support.

The support (Pr_2O_3) was synthesized following established procedure from literature (Ay and Üner, 2015). Prior to applying all three synthesis methods, the required $Pr(NO_3)_3.6H_2O$ salt was mixed in distilled water. The solution was stirred for 3 h and dried for 24 h at 110 °C. Post drying, the sample was placed in a furnace and calcined at 600 °C for 4 h to yield the Pr_2O_3 support.

2.1.2. Incipient Wetness Impregnation (IWI) Method

A batch of 20 wt.% Ni/Pr_2O_3 was synthesized using the IWI method previously reported in (Singh et al. 2018; Jawad et al. 2020). The Ni metallic salt used was dissolved in distilled water. The aqueous metallic salt was then

used to impregnate the already prepared Pr_2O_3 support. It should be noted that when using the IWI method, the volume of the impregnating solution must be the same as the support's pore volume. The mixture was dried overnight at about 100 – 120 °C, before the sample was calcined for 5 h at 850 °C using 5 °C min^{-1} ramping rate. The resulting material was then grounded and sieved to the desirable size (140 -250 μm).

2.1.3. Ultrasonic Assisted Impregnation Synthesis (US-WI) Method.

Ultrasonic assisted wet impregnation (US-WI) method was utilized using an ultrasonic generator furnished with a probe (Roslan et al. 2022) (Setiabudi et al. 2018). The required Ni nitrate salt needed to synthesize 20 wt.% Ni/Pr_2O_2 catalyst was mixed in distilled water twice the quantity of Ni nitrate salt. The salt solution was mixed in an ultrasonic bath for about 5 min. The support (Pr_2O_3) was then added to the resulting solution and continuously mixed using the ultrasonic bath at 80 °C until a paste-like form of the mixture was obtained. The obtained paste was dried for about 24 h at around 110 °C to eradicate all traces of water molecules before calcination at 850 °C at 5 °C min^{-1}. This step was followed by grinding and sieving of the calcined material to the desired size (140 - 250 μm).

2.1.4. Pechini Sol-Gel (PSG) Synthesis Method

The PSG method employed to prepare 20 wt.% Ni/Pr_2O_3 was adopted from previous studies (Pechini et al. 1967; Kakihana 1996; Khalil 2003; Mishra et al. 2019). The process entails the in-situ polymerization of the sol-gel process by adding ethylene glycol. The Ni nitrate salt and synthesized support (Pr_2O_3) was dissolved at ambient conditions in 2 M citric acid solution with 2:1 citric acid to metal molar ratio. The role of citric acid as a chelating agent was to assist homogeneous distribution of metal, and to create a segregate from the solution. In addition, ethylene glycol was added as a complexing agent to the solution in a 2:1 ratio of citric acid to ethylene glycol. The sample mixture was subsequently stirred at 25 °C for 2 h and ammonia was added to adjust the pH to become less acidic. Heat was applied to the resulting mixture at 80 °C for 4 h and continuously stirred. The formulated gel was oven-dried at 110 °C. The grounded form of the xerogel material was obtained using an agate crucible before annealing at 850 °C for 5 h at 5 °Cmin^{-1}. The calcined material was further grounded and sieved to the desirable size (140 -250 μm).

2.2. Catalyst Characterization

The physical properties of all the catalysts were obtained using the N_2 physisorption analyses. The data was analyzed and processed by a Thermo Scientific acquisition analyzer which is furnished with a degasser station and a surfer acquisition (version 1.2.1) software. The crystalline structure was evaluated by powder X-ray diffraction (XRD) measurements with Cu Kα radiation (λ = 0.154 nm). The range of the analysis using a Rigaku Miniflex II instrument was recorded at 2θ = 2º - 70º at a rate of 0.02º over 2 s. This procedure was followed by matching the peaks with known structures in the Inorganic Crystal Structure Database (ICSD). Also, the particle crystallite size for all 20 wt.% Ni/Pr_2O_3 catalysts synthesized by the IWI, US-WI and PSG methods were computed employing the Williamson-Hall model shown in Eq.1 (Himabindu et al. 2021) (Khorsand Zak et al. 2011).

$$\beta_{hkl}\cos\theta = \frac{P\lambda}{D_{hkl}} + (4\varepsilon\sin\theta) \qquad (1)$$

Where θ and λ (Cu Kα) are the Bragg angles of diffraction, and wavelength, respectively, β_{hkl} is the peak width at half-maximum intensity, P is the shape factor (0.9) and D_{hkl} is the crystallite size of the 20 wt.% Ni/Pr_2O_3 catalysts.

The binding energy and surface composition for the calcined catalysts (wide and narrow scan) were obtained using X-ray photoelectron spectroscopy (XPS). The peak intensities and atomic percentages were obtained using the estimated Gaussian and Lorentzian lines and the intensity ratios. The equipment employed was the PHI-5000 VersaProbe spectrometer which had a hemispherical electron analyzer.

The catalysts morphologies and composition of each element were evaluated at 15× magnifications using the field emission scanning electron microscope (FESEM) (Schottky-type field emission cathode beam). Resolution images of the catalysts were captured, and the inner shell electrons were excited to obtain the composition of the elements. Energy Dispersive X-ray (EDX) was also used to confirm the presence and composition of elements used for the catalyst's synthesis. The primary composition of the catalyst was obtained by EDX, when inner shell electrons were excited, hence forming specific X-rays with suitable intensity for the analytical data.

A Thermo Scientific Analyzer -TPDRO 1100, was used to ascertain the reduction capacity of the 20 wt.% Ni/Pr_2O_3 catalysts samples synthesized by IWI, US-WI, and PSG methods. Pretreatment of about 100 mg of fresh samples was carried out in a 30 mL min^{-1} flow of Ar at a 10 ºC min^{-1} heating rate until about 300 ºC and held for 0.5 h. Reduction of the pretreated catalysts with 30 mL min^{-1} of 10% H_2 in Ar carrier gas was carried out at 900 ºC (at 10 ºC min^{-1}) and held for 60 min before subsequently cooled to ambient temperature.

The morphologies of the micro-structures of the calcined and spent Ni/Pr_2O_3 were obtained by transmission electron microscopy (TEM) (JEOL JEM-2100) at 5,000× magnifications. During the process, various features of the catalyst material were visibly observed.

The solid-state thermal profile of the spent catalysts was obtained by thermogravimetric analysis (TGA) using a TA instrument (Q 500 series). The weight loss (TG) and the derivative weight loss (DTG) of the catalysts were obtained between 25 ºC – 900 ºC at 10 ºCmin^{-1} in mixed 80 % N_2 and 20 % O_2 flow.

2.3. Catalytic Activity Test

A fixed bed reactor in a gas manifold station, and a gas chromatography (GC) instrument was used to conduct the experiment and analyze results from the experimental runs. The GC which was employed to detect unconverted reactants gases (CH_4, CO_2) and products (H_2 and CO) at the outlet stream, was operated using He (20 $mLmin^{-1}$) with the temperature of the column at 150 ºC. The reactor (inner diameter of 10 mm) was packed with the catalyst (0.1 g) and all experiment were repeated thrice to eliminate errors. Pre-reaction, reduction of the fresh catalysts was carried out in a 50% H_2/N_2 flow (60 $mLmin^{-1}$) for 1 h at 800 ºC (for uniformity) with a ramping of 5 ºC min^{-1}. Post-reduction step, the reactor was flushed with N_2 gas while setting the desired reaction temperature. Transport phenomena were minimized by ensuring the catalysts particles are sieved to the desired range 140 – 250 µm. More also, the gas hourly space velocity (GHSV) was set at about 30,000 h^{-1} to ensure the transport effects were insignificant. The total pressure of 1 bar with reaction temperature ranged 600 - 950 ºC was employed during the reaction, while N_2 was used throughout the study as a diluent gas. Using feed flow rates and exit gas composition, the reactants conversion and product ratio were obtained using Eqs. (2 - 4) (Moradi et al. 2014). The schematic of the experimental rig for the MDR reaction to produce syngas is represented in Fig. 1.

$$X_{CH_4}\% = \frac{F_{CH_4\,(in)} - F_{CH_4\,(out)}}{F_{CH_4\,(in)}} \times 100 \qquad (2)$$

$$X_{CO_2}\% = \frac{F_{CO_2\,(in)} - F_{CO_2\,(out)}}{F_{CO_2\,(in)}} \times 100 \quad (3)$$

$$\frac{H_2}{CO}\text{ratio} = \frac{F_{H_2(out)}}{F_{CO_{(out)}}} \quad (4)$$

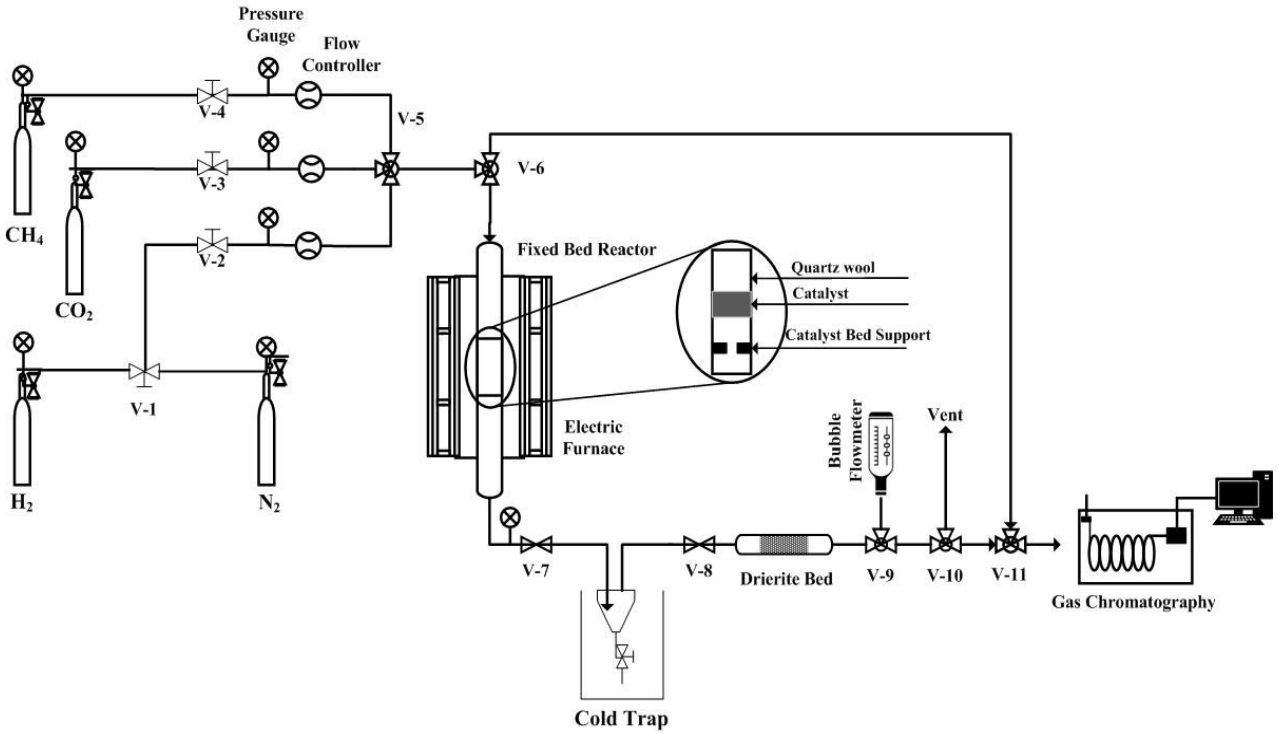

Fig. 1 Schematic representation of the MDR experimental rig

3. Results and Discussions

3.1 Catalyst Characterization

BET Analysis

The textural characteristics of the 20 wt.% Ni/Pr_2O_3 catalysts synthesized by incipient wetness impregnation (IWI), ultrasonic-assisted wet impregnation (US-WI) and Pechini sol-gel (PSG) method are shown in Table 1. From the table, a reduction in the BET surface area and pore volume was found in the order; US-WI, IWI, and PSG (for the 20wt% Ni/Pr_2O_3 catalysts). The IWI and US-WI synthesized catalyst had very similar pore volume compared to the PSG catalyst. The average pore size of the catalysts reduced in the order IWI, US-WI, and PSG for the synthesized catalyst. This pattern is linked to the formation of the Pr_2O_3 support's pore structure in the presence of NiO at the catalyst's surface. Referring to the IUPAC sorption isotherms, the IWI, US-WI, and PSG synthesized 20wt% Ni/Pr_2O_3 catalysts exhibited type H2 hysteresis loop from a type IV curve thereby revealing the mesoporosity of the synthesized catalyst materials.

Table 1 Textural properties of calcined the 20wt% Ni/Pr_2O_3.

Catalyst (20wt% Ni/Pr_2O_3)	**BET Surface Area ($m^2\ g^{-1}$)**	**pore volume ($cm^3\ g^{-1}$)**	**Average pore size (nm)**
IWI	6.7	1.28×10^{-2}	7.6

US-WI	8.9	1.29×10^{-2}	5.8
PSG	7.3	9.95×10^{-3}	5.5

XRD Analysis

Diffractogram of the 20 wt.% Ni/Pr_2O_3 catalysts synthesized by incipient wetness impregnation (IWI), ultrasonic-assisted wet impregnation (US-WI) and Pechini sol-gel (PSG) method are shown in Fig. 2. Peaks matching the XRD data for NiO (PDF 00-001-1239 for PSG synthesized catalyst, PDF 01-089-7131 for IWI and US-WI synthesized catalysts, respectively), Pr_2O_3 (PDF 00-061-0049 for PSG catalyst, PDF 00-006-0410 for IWI catalyst and US-WI synthesized catalysts, respectively) and PrO_2 (PDF 00-024-1006 for IWI and US-WI synthesized catalysts, respectively) are visible on the diffractogram. Interestingly, The PSG synthesized catalysts formed the partially oxidized Pr_6O_{11} species phase (PDF 00-041-1219). There were overlap of the Pr_2O_3 (Pr^{3+}) and PrO_2 (Pr^{4+}) phase species for IWI and US-WI synthesized catalysts while Pr_2O_3 (Pr^{3+}) and Pr_6O_{11} (Pr^{3+} and Pr^{4+}) phases overlapped for the PSG synthesized catalyst. The ease with which Pr^{3+}/ Pr^{4+} redox couples are formed is likely responsible for the co-existence and overlapping behaviour of the support (Ahn et al. 2012; Milberg et al. 2017). Furthermore, the formation of Pr_6O_{11} phase species for the PSG-Ni/Pr_2O_3 catalyst as against the PrO_2 phase species for the IWI and US-WI catalyst might be responsible for easier release of oxygen molecules which would aid carbon gasification. Different support structure of the same species could potentially present different ability to gasify carbon. This is so because the Pr_6O_{11} is less stable when compared to the PrO_2 species, hence, the Pr_6O_{11} species can easily release oxygen ions for the carbon gasification process as compared to the PrO_2 which was present in the IWI and US-WI catalysts. More also, the PSG catalyst presents additional Pr species with additional 11 oxygen atoms (Pr_6O_{11}) while the IWI and US-WI have additional Pr species with 2 oxygen atoms (PrO_2).

The Williamson-Hall model was used to fit XRD data to obtain the nano crystallite size of the samples. As shown in Fig. 3, $\beta_{hkl}\cos\theta$ was plotted against $4\sin\theta$ using the preferred peaks of the 20 wt% Ni/Pr_2O_3 catalyst. The gradient of the fitted data denoting the strain (ε) was -0.0007, -0.0007 and -0.0015, respectively, while the y-intercept was 0.0065, 0.0065 and 0.0131, for the IWI, US-WI, and PSG catalysts, respectively. From Eq.1, the values for the particle crystallite size were calculated as 21.3 nm, 21.3 nm, and 10.6 nm, for the IWI, US-WI, and PSG catalysts, respectively. This trend agrees with literature where the crystallite size of Ni catalysts is established to be in the range of 10 – 20 nm (Luisetto et al. 2015; Goula et al. 2016).

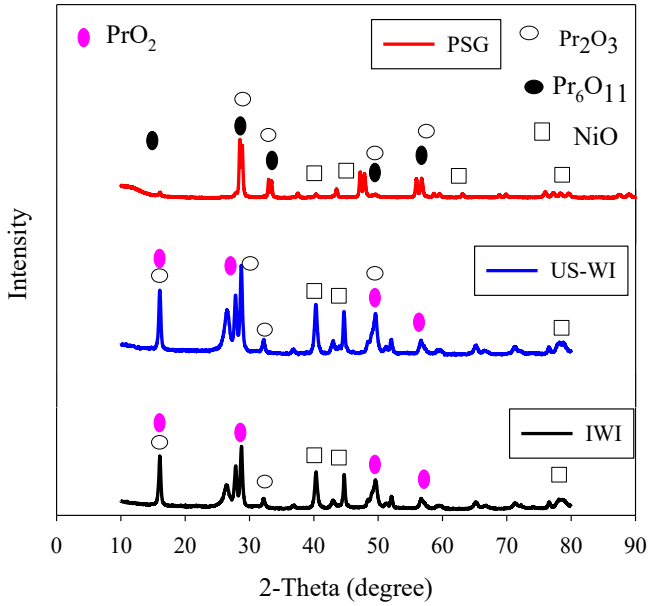

Fig. 2 X-ray diffractogram of the fresh 20 wt.% Ni/Pr_2O_3 catalysts.

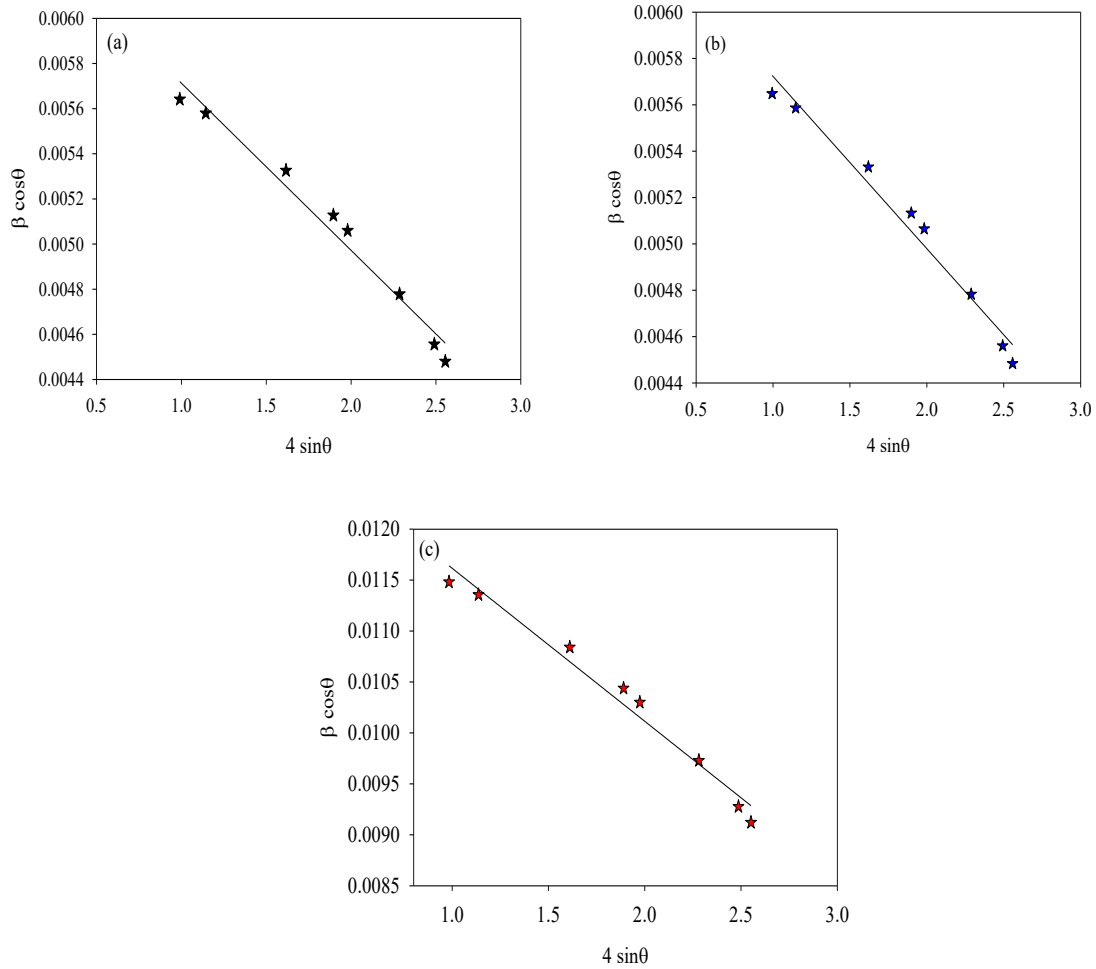

Fig. 3 Williamson-Hall analysis for 20 wt. % Ni/Pr_2O_3 catalyst a) IWI b) US-WI c) PSG synthesis methods.

XPS Analysis

Wide and narrow scans of the XPS analyses of the calcined 20 wt.% Ni/Pr_2O_3 catalyst for the IWI, US-WI, and PSG methods are represented in Fig. 4 a-c. Ni (19.26 %), Pr (20.26 %) and O (60.5 %) species can be found in the wide spectra and the data agree with the catalyst's formulations employed for the various synthesis methods. Furthermore, the main binding energy of Ni peaks corresponding to $2p_3$, and $2p_1$ are seen around 855 and 853 eV, respectively. This indicates the presence of Ni as Ni^{2+} forming NiO (Leclercq et al. 1998; Kim et al. 2007). Peaks representing binding energies corresponding to Pr3d5 and Pr3d3 species are present in the IWI, US-WI, and the PSG catalysts (Milberg et al. 2017) (Song et al. 2007). The finding agrees with the XRD data (Fig. 2), which confirms the presence of two different Pr phase for IWI and US-WI catalysts (Pr_2O_3 and PrO_2) and PSG catalyst (Pr_2O_3 and Pr_6O_{11}) respectively.

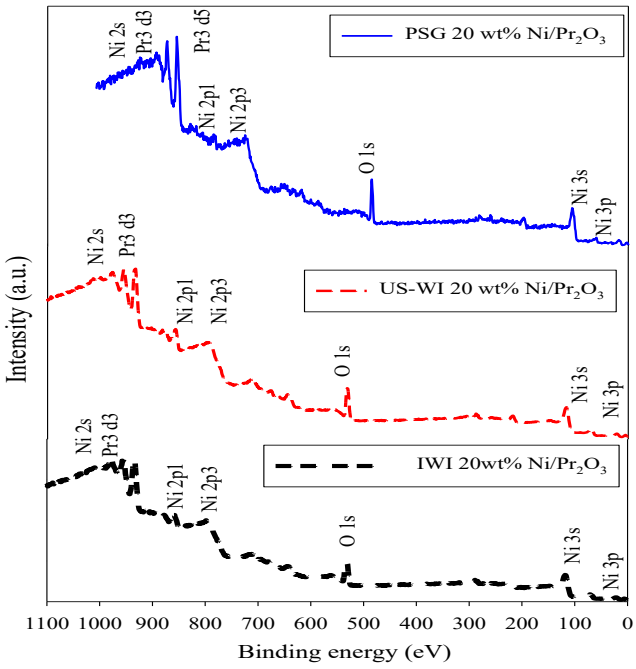

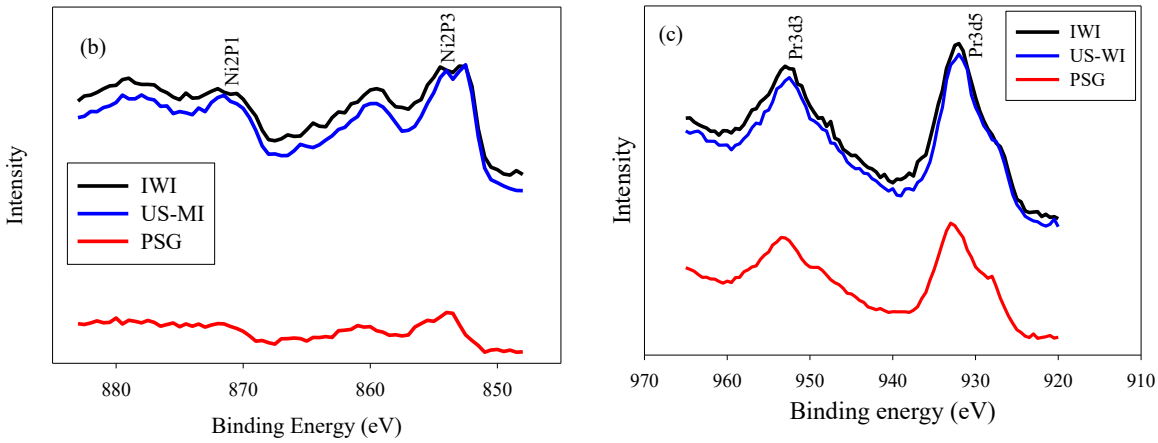

Fig. 4 XPS profile of the (a) calcined 20 wt% Ni/Pr_2O_3 catalysts (b) narrow scan Ni2P1 and Ni2P3 peaks (c) narrow scan Pr3d3 and Pr3d5 peaks for the 20 wt% Ni/Pr_2O_3 catalysts.

Species of O_2 in the 20 wt% Ni/Pr_2O_3 Catalyst

XPS analysis can estimate the quantity and type of surface O_2 species in heterogeneous catalysts. O 1s XPS spectra for the 20 wt.% Ni/Pr_2O_3 catalysts synthesized via IWI, US-WI and PSG methods are shown in Fig. 5. O 1s species linked to the lattice and adsorbed oxygen can be seen at binding energy of 529 eV and 531 eV, respectively (Kuhn and Ozkan 2008). Upon analysis of the O 1s XPS spectra, dual peaks representing dual oxygen species were present: adsorbed oxygen species (O_A) and lattice oxygen species (O_L). According to Lee et al., (2018), O_A species are generated via oxygen atoms adsorbed into the oxygen vacancies created by the desorbed mobile lattice oxygen vacated from the bulk of the catalysts. These vacancies are created when O_L species from the catalyst support oxidizes the reactants (cracked CH_4 to form carbon), thereby creating vacant oxygen sites in the catalyst.

The relative amount ratio of O_L to O_A was determined using the XPS areas of the peaks for different preparation methods. The result showed that the O_L to O_A ratio increased in the preparation method order: IWI (0.75) ~ US-WI (0.75) > PSG (0.86). More also, the PSG catalyst had near equal amount of O_L and O_A species suggestive of a balance between the oxygen species. This has potentially contributed to the better performance (in terms of stability) of the PSG catalyst when compared to the catalysts from the other synthesis methods (IWI and US-WI).

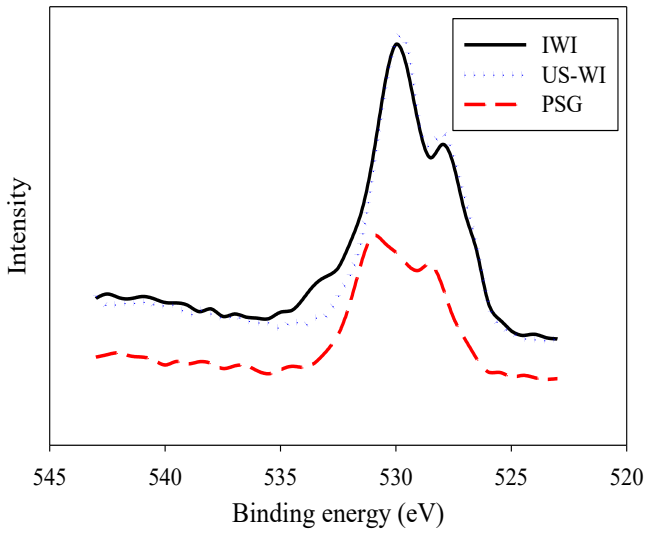

Fig. 5 XPS spectra for the narrow O 1s peaks for the 20 wt.% Ni/Pr_2O_3 catalysts.

FESEM Analysis

Micrographs (15,000 × magnifications) of the fresh samples from the various synthesis procedures (IWI, US-WI, and PSG) is represented in Fig. 6(a-c). The smoothness and uniformity of the sample catalysts are in increasing order from Fig. 6a Fig. *6*c. This supports higher degree of dispersion and stronger interaction in the sample prepared by PSG method. Also, upon visual inspection, the metal particles in the US-WI synthesized catalyst appears to be more uniform as against the sample synthesized by IWI method. However, FESEM images alone are not sufficient to make conclusive statements on the various catalysts' material.

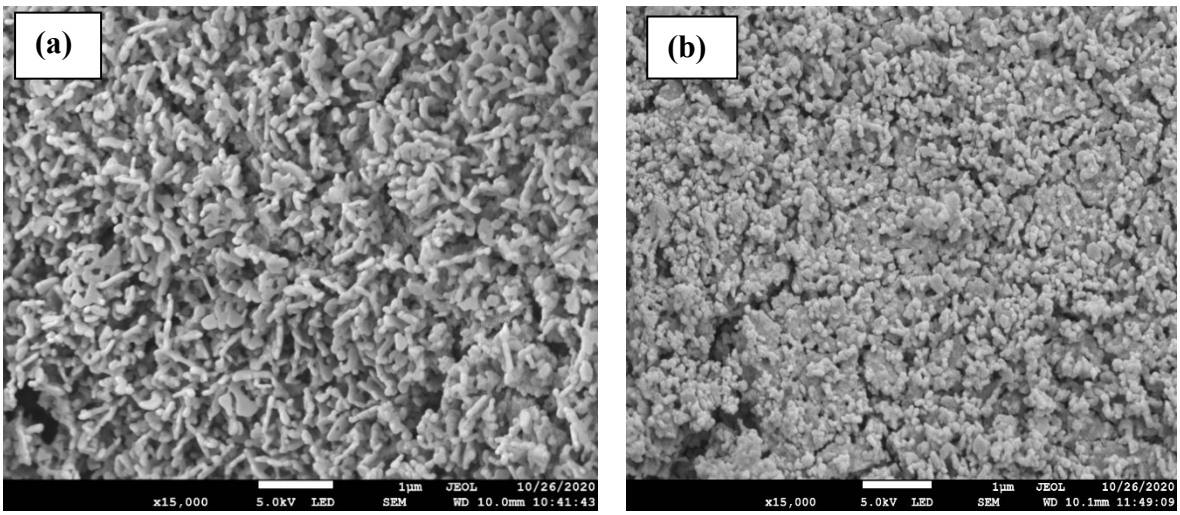

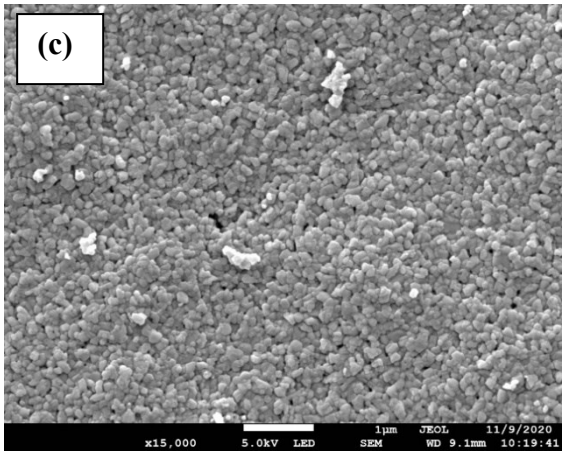

Fig. 6 FESEM images (15,000 magnifications) of the 20wt% Ni/Pr_2O_3 synthesized by a) IWI b) US-WI c) PSG methods.

EDX Analysis

EDX analysis of the calcined 20 wt.% Ni/Pr_2O_3 synthesized by IWI, US-WI and PSG methods are represented in Fig. 7(a-c). Using the EDX analysis, it is difficult to spot the best synthesis method. However, the mapping reveals the presence of Ni, Pr, and O, which are the major components of the catalyst used in this study. The atomic percentage composition of the Ni, Pr, and O are 22 %, 17 %, and 61 %, for the IWI, 17 %, 20 %, and 63 for the US-WI and 13 %, 17 % and 70 % for the PSG synthesized catalysts, respectively. This composition explains the degree of effectiveness of the synthesis methods in obtaining the specific catalyst material.

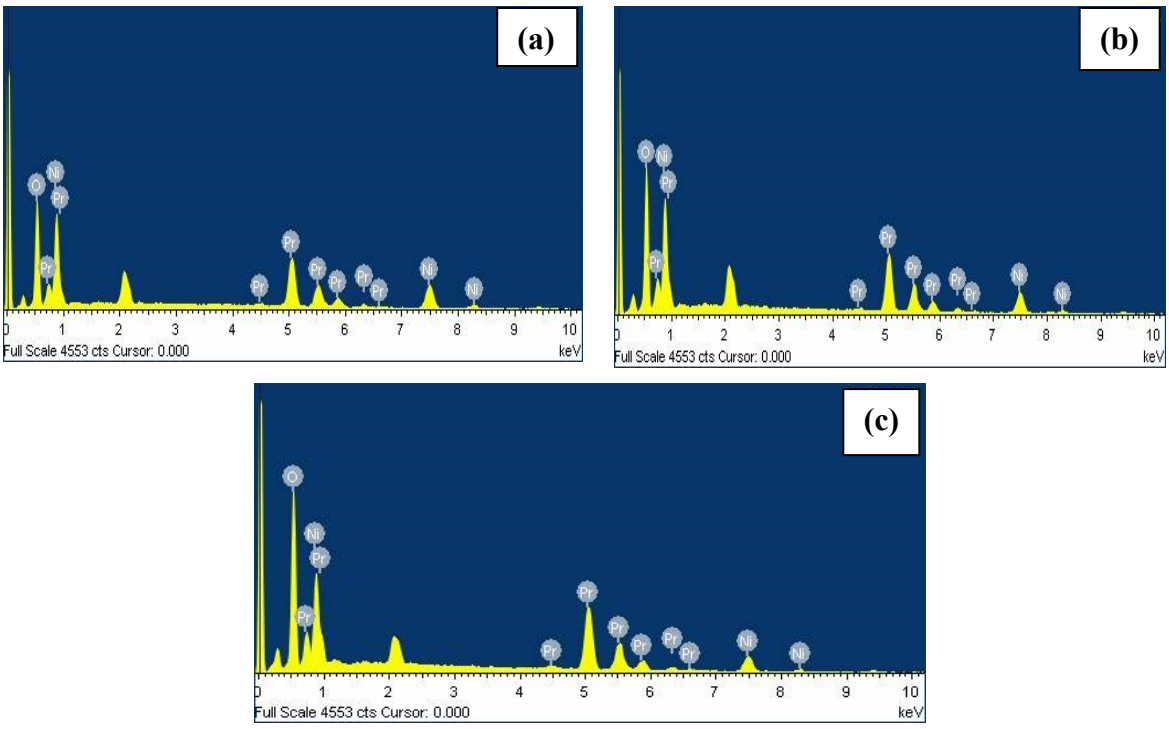

Fig. 7 EDX analysis of the 20 wt.% Ni/Pr_2O_3 synthesized by a) IWI, b) US-WI c) PSG methods.

3.2 Catalyst Activity

Effects of Synthesis Methods on Conversion

Table 2 and Table 3 depicts the dependence of the Average feedstocks' (CH_4 and CO_2) conversion on the catalyst's synthesis methods, i.e., IWI, US-WI, and PSG methods. These experiments were conducted at 800 ºC for 2 h for all synthesis methods. The catalytic test revealed that the average CH_4 conversions were approximately 88 % for the IWI, US-WI, and PSG synthesized catalysts, while average CO_2 conversions were 87.5%, 90% and 92%, respectively, for the IWI, US-WI, and PSG synthesized catalysts. The conversions of CH_4 and CO_2 for IWI and US-WI methods had similar behavior with respect to the catalyst behavior during the time of reaction. CH_4 and CO_2 conversion for the IWI and US-WI methods were stable until after 1 h, and then slowly eroded until the reactant flow completely stopped at around 2 h due to carbon blockage of the reactor's flow line.

According to Deraz, (2018) in the impregnation method, an appropriate amount of the metal precursor is mixed via diffusional means with the support phase before drying takes place. During the process of diffusion, the overall solution changes thereby releasing heat in a short period (Osazuwa et al. 2021). Also, Jiang, (2006) reported that when the IWI synthesis method is applied, sintering and particles size growth is very likely because the metal and oxide phases possess very high surface energy. Therefore, during this experiment, it is likely that the sudden restriction of flow after 1 h can be attributed to sintering of the metallic particles followed by carbon buildup that block the reactor flow lines since the catalysts were made up of high oxide loading of Pr_2O_3 and its stable species (PrO_2) as described in the XRD data in Fig. 2. More also, with reference to the synthesis method, catalysts synthesized by the IWI method were likely not homogenously dispersed. Nevertheless, the IWI method can effectively control the capacity of active components. Hence, the method is generally effective when there are no exact particle size requirements but its poor active metal dispersity and uneven distribution of particle size are some of the inherent challenges associated with this technique (Zhang et al. 2014).

Researchers have tried to enhance this technique by introducing several variations, such as increasing the uniformity of dispersion by employing ultrasonic wave (Setiabudi et al. 2018). This technique uses the cavitation of ultrasound wave to achieve the uniform dispersion of metals in the support (Passos et al. 2005). The cavitation nuclear bubble breakdown generates a local temperature, pressure, impact wave and a micro jet, thereby creating a new and unique physicochemical environment that cannot be achieved during the simple impregnation procedure (Zhang et al. 2014). However, in the current experiment, the ultrasonic wave assisted wetness impregnation did not improve the 20 wt.% Ni/Pr_2O_3 catalyst's performance possibly due to the loading of metal employed.

For the PSG synthesis method, CH_4 conversion increased slightly from about 86 % to 89 %, and CO_2 conversion increased from 88 % to 97 % after 1 h before dropping slightly to 90 % after 2 h time on stream (TOS). During the catalyst synthesis using PSG method, citric acid and ethylene glycol undergo esterification reaction (Lin et al. 2007). The organic structure breakdown due to heating is inhibited to alter the formation of the resulting catalyst and its physicochemical properties. Furthermore, the non-dependence on the process conditions resulting from positively charged ions in the formulated catalyst and the low temperature treatment ensures sintering is eliminated. Hence, initial pressure buildup due to carbon deposits was not observed as the catalyst remained active. Extensive studies and reviews have been published on the PSG method (Dimesso 2018; Osazuwa et al. 2021), while other researchers have found the application of this method highly productive (Majid et al. 2005; Jana et al. 2010; Shin et al. 2018; Bai et al. 2019). For instance, Majid et al., (2005) successfully synthesized SrFeOx catalysts using the PSG method. The method produced higher quality material which possessed better catalytic

properties. Shin et al., (2018) synthesized Ni/ZrO_2-Al_2O_3 catalyst for MDR reaction and carried out a comparative study using the PSG and other synthesis methods. The synthesized PSG catalyst had the highest stability under the given experimental conditions. According to Danks et al., (2016), the dissolution of the metallic salt, citric acid, and ethyl glycol in water created a homogenous mixture. Hence, the introduction of heat activated the poly-esterification reaction to form a polymer matrix before the final calcination of the polymeric structure.

Table 2 Average CH_4 Conversion obtained for IWI, US-WI, and PSG catalysts over TOS.

	CH_4 conversion		
Time (h)	**20 wt% Ni/Pr_2O_3 catalyst synthesize by the IWI method.**	**20 wt% Ni/Pr_2O_3 catalyst synthesize by US-WI method.**	**20 wt% Ni/Pr_2O_3 catalyst synthesize by PSG method.**
0.5	88	88	86
1	88	88	88
2	carbon blockage of the reactor flow line	carbon blockage of the reactor flow line	89

Table 3 Average CO_2 Conversion obtained for IWI, US-WI, and PSG catalysts over TOS

	CO_2 conversion		
Time (h)	**20 wt.% Ni/Pr_2O_3 catalyst synthesize by the IWI method.**	**20 wt.% Ni/Pr_2O_3 catalyst synthesize by US-WI method.**	**20 wt.% Ni/Pr_2O_3 catalyst synthesize by PSG method.**
0.5	88	90	88
1	87	90	97
2	carbon blockage of the reactor flow line	carbon blockage of the reactor flow line	90

Determination of the Effective Reaction Temperature

Fig. 8 (a-c) represents the temperature effects study on the MDR reaction in the temperature range 600 ºC – 950 ºC. The study was carried out by employing the PSG- 20 wt.% Ni/Pr_2O_3 catalysts because this catalyst gave the best result during the preliminary study. The study showed that an increase in reaction temperature has a direct relationship with the MDR reaction. From each experimental run, the conversion of CH_4 (Fig. 8a) and CO_2 (Fig. 8b) were relatively constant with an increase in time for the entire 8 h TOS. The highest CH_4 conversions at 600, 700, 800, 900, and 950 ºC were approximately 47 %, 56 %, 89 %, 97 %, and 97 %, respectively, while the highest CO_2 conversion at 600, 700, 800, 900, and 950 ºC, were 46 %, 54 %, 89 %, 98 %, 99 % respectively. The MDR reaction is accompanied by various side reactions that can alter the reaction performance depending on the overall reaction conditions. At 600 °C (lower temperature), MDR is controlled by the water gas shift (WGS) reaction. At 950 °C (higher temperature range), the net WGS reaction becomes negligible and the backward reaction (the reverse water gas shift (RWGS) reaction shown in Eq. 5) dominates (Lee et al. 2014; Nabgan et al. 2016).

$$CO_{2(g)} + H_{2(g)} \leftrightarrow CO_{(g)} + H_2O_{(g)} \qquad \Delta H^{\circ}{}_{298K} = 41\ kJmol^{-1} \quad (5)$$

When the temperature is high, the RWGS reaction uses up the reactant (CO_2) and product (H_2) while the WGS reaction at low temperature consumes the product (CO). This justifies the high CO_2 conversion (approximately 100 %) observed at 900 and 950 °C in this study, as shown in Fig. 8b. Hence, to eradicate the effect of the various side reaction on the overall outcome, the MDR reaction is often investigated between 700 – 900 °C. At these conditions, the effects of side reactions are negligible because the catalytically driven CH_4 cracking/reforming is dominant.

Another side reaction that often accompanies MDR reaction is the Boudouard reaction, also known as gasification of char and it is represented in Eq. 6 (Wang et al. 1996; Fan et al. 2009).

$$2CO_{(g)} \leftrightarrow CO_{2_{(g)}} + C_{(S)} \qquad \Delta H^{\circ}{}_{298K} = -172\ kJmol^{-1} \qquad (6)$$

During the MDR reaction, the Boudouard reaction proceeds at low temperature (< 600 °C) with the decomposition of CO to yield C and CO_2. This is due to the large enthalpy, which shifts the equilibrium towards the decomposition of CO rather than its formation. Nonetheless, when the entropy terms become significant during the reaction, the free energy becomes negative and the reverse Boudouard reaction dominates. Hence, at low temperature conditions, Boudouard reaction is the major carbon source while at higher temperature, the carbon produced is from CH_4 cracking (Baharudin et al. 2022), (Lovell et al. 2017). With reference to Fig. 8b, at higher temperature conditions (> 900 °C), CO_2 is almost completely used up (about 99 % conversion) to form C and CO in the reverse Boudouard process.

Fig. 8 c shows the product ratio (syngas ratio) plotted against time for the process over PSG- 20 wt% Ni/Pr_2O_3 catalyst. Overall, the ratio falls between 0.8 – 1.2. The effect of temperature on the syngas ratio is not significant. At lower temperature i.e., 600 ºC, the syngas ratio was about 0.8 while at higher temperature, i.e., > 900 ºC, it shifts slightly to about 1.2. According to De Caprariis et al., (2016), syngas with unity ratio is more desirable as feedstock for fuel production processes. H_2: CO ratio > 1 indicates the dominance of the Boudouard reaction or hydrocarbon cracking where CO is used up, whereas H_2: CO < 1 indicates that the RWGS reaction has occurred where H_2 and CO_2 are consumed (Lovell et al. 2017).

The MDR reaction using the PSG synthesized 20 wt.% Ni/Pr_2O_3 catalyst was endothermic in nature; hence it obeyed the Arrhenius equation with respect to its temperature dependency. During the reaction TOS at a temperature ranging from 600 – 900 ºC, there was a steady increase in reactants conversion. However, from > 900 ºC, the conversion remained constant due to continuous CH_4 cracking, which dominated as against the Boudouard reaction (Khajenoori et al. 2015).

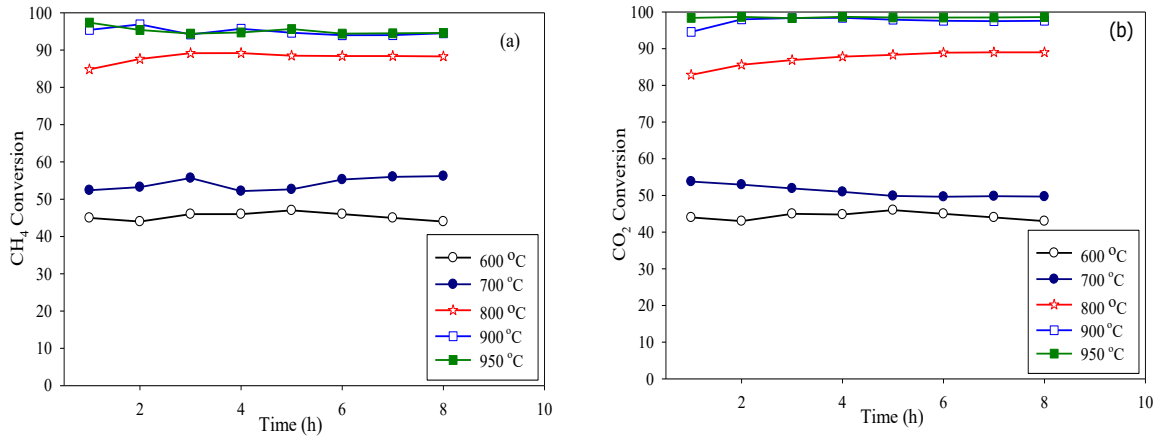

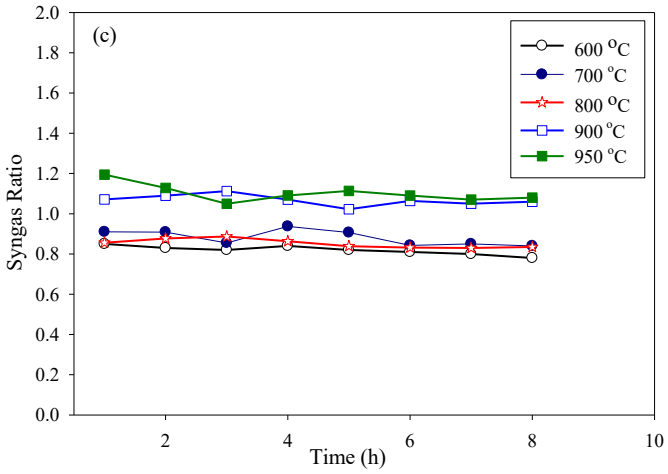

Fig. 8 Temperature effects on MDR reaction over PSG- 20 wt.% Ni/Pr_2O_3 a) Average CH_4 b) Average CO_2 conversion c) syngas ratio (H_2: CO).

3.3 Carbon Study.

Stability Study.

The stability of the MDR reaction over PSG- 20 wt.% Ni/Pr_2O_3 catalyst for about 24 h is represented in Fig. 9. This catalyst (PSG- 20 wt.% Ni/Pr_2O_3) has been selected for the stability study since it gave the best result in terms of conversion when compared to the IWI and US-WI catalysts. The average reactants' conversion during the stability test was approximately 80 % and 86 % for CH_4 and CO_2, respectively. Also, the catalyst experienced slight deactivation over 24 h TOS, with the percentage of deactivation in terms of CH_4 conversion about 16 %, while CO_2 conversion was 12 %. However, the overall volumetric flow of the outlet gas completely seized after about 24 h due to blockage of the reactor tube due to excess carbon. This means that over the TOS, the catalyst lost its activity, and possessed limited numbers of active sites to continually convert the reactants gases to gaseous H_2 and CO. Hence, the amount of deposited carbon was in excess of the amount of carbon being converted. The carbon deposits encapsulated the metallic site, thereby deactivating the catalyst over 24 h, which eventually resulted in blockage of the reactor. It would be interesting to further study on the effects of promoter on the stability of the PSG- 20wt% Ni/Pr_2O_3 catalyst as a means to enhance its stability.

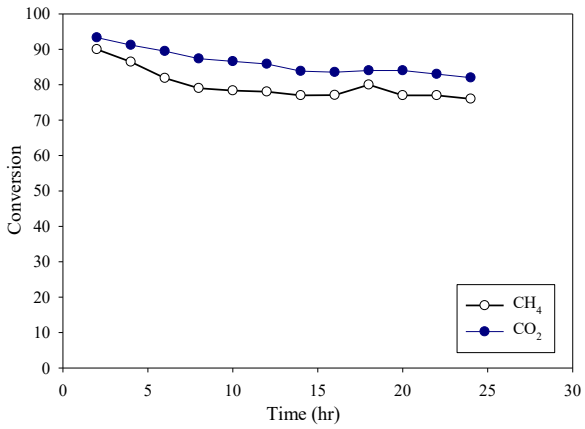

Fig. 9 Stability of MDR reaction over PSG- 20 wt.% Ni/Pr_2O_3 catalyst.

3.4 Used Catalyst Characterization.

The XRD profile of the spent 20 wt.% Ni/Pr_2O_3 catalyst (synthesized via the IWI, US-WI, and PSG method) is represented in Fig. 10. It can be observed that peaks representing metallic Ni, and Pr_2O_3 were found in all spent catalysts. The crystalline structure of metallic Ni (PDF 03-065-2865) was cubic, while the Pr_2O_3, (PDF 01-078-0309) and carbon were hexagonal in nature. Peaks ascribed to the presence of carbon matching the hexagonal crystalline phase (PDF 01-081-9116) were present in all catalysts. The main carbon peak in the PSG- 20 wt.% Ni/Pr_2O_3 was less pronounced which could explain its higher stability when compared to the IWI and US-WI 20 wt.% Pr_2O_3 catalysts. Also, although the IWI and US-Wi 20 wt.% Pr_2O_3 catalysts experienced high CH_4 cracking there was lesser carbon gasification occurring as compared to the PSG- 20 wt.% Ni/Pr_2O_3 catalyst which had a better ability to resist deactivation and pressure buildup in the reactor (which was caused by excess carbon deposits) after 2 h.

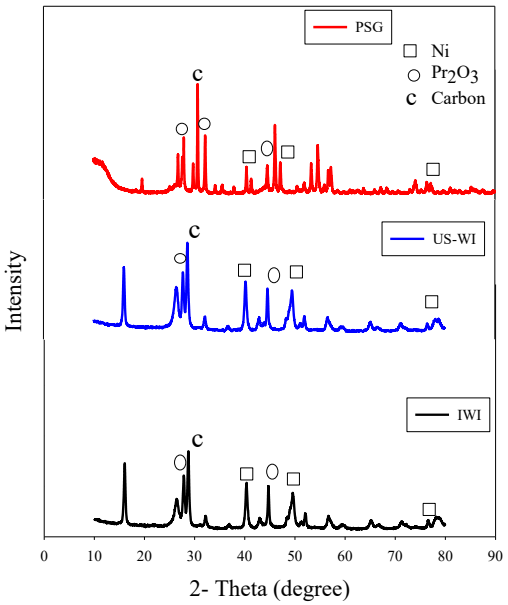

Fig. 10 X-ray diffractogram for the spent PSG-20 wt.% Ni/Pr_2O_3 catalysts

Representative FESEM images of the spent IWI, US-WI, and PSG 20 wt. % Ni/Pr_2O_3 catalysts at 15,000 × magnifications are shown in Fig. 11 (a-c). All catalysts showed visibly pronounced carbon filaments with the IWI and US-WI catalysts showing some form of agglomeration or encapsulation of metallic particles (refer to Fig. 11 (a and b)). The PSG-20 wt.% Ni/Pr_2O_3 catalyst represented in Fig. 11c had less agglomeration. Also, upon visible inspection, the particles (indicated in red circles) are smaller in size when compared to the particles of the IWI and US-WI catalysts. The result strongly corroborates with the XRD represented in Fig. 10 for all spent catalysts which showed evidence of carbon formation.

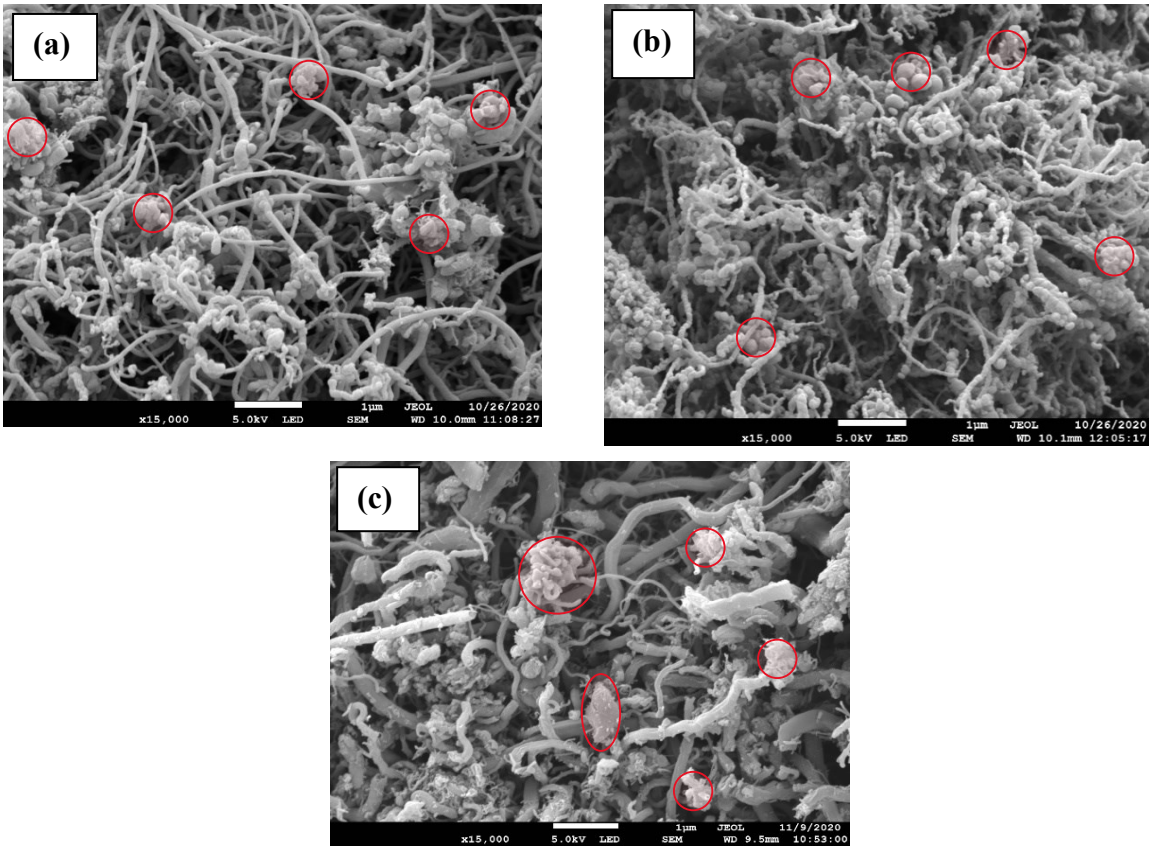

Fig. 11 FESEM images of the 20 wt.% Ni/Pr_2O_3 catalyst synthesized by a) IWI b) US-WI c) PSG methods (15,000 × magnifications).

To further prove the existence of carbon and the specific carbon types in the various spent catalysts, TEM images represented in Fig. 12(a-c) were captured. The images show various degrees of carbon formation for the different synthesis methods. In Fig. 12a and b representing the catalysts synthesized by the IWI and US-WI methods, two carbon types exist. The carbon species are visibly described by the thin elongated tube-like structures (identified as the red arrows) and the darker shade round-like structures (identified as the red circles) which encapsulate the Ni metal, making them clog together. For MDR reaction to proceed, the carbon is produced via CH_4 cracking which deactivates the catalysts and subsequently blocks the reactor tube if not converted in-situ reaction. The encapsulated round-like carbon reported by Son et al., (2014) as graphitic carbon are found on the metal surface phase or accumulates in the reactor tube. When deposited on the metal surface, they deactivate the metal catalyst, while as deposits in the reactor tubes, they block the flow of reactants through the reactor. Spent PSG- 20 wt.% Ni/Pr_2O_3 represented in Fig. 12c shows obvious thin elongated tube-like carbon nanotubes and very minimal encapsulating round-like (graphitic) carbon after 2 h TOS. Also, the Ni metallic particles (identified as the blue circles) were still visible in the spent PSG- 20 wt.% Ni/Pr_2O_3 sample as it ensured the catalyst remained active and stable over the reaction TOS.

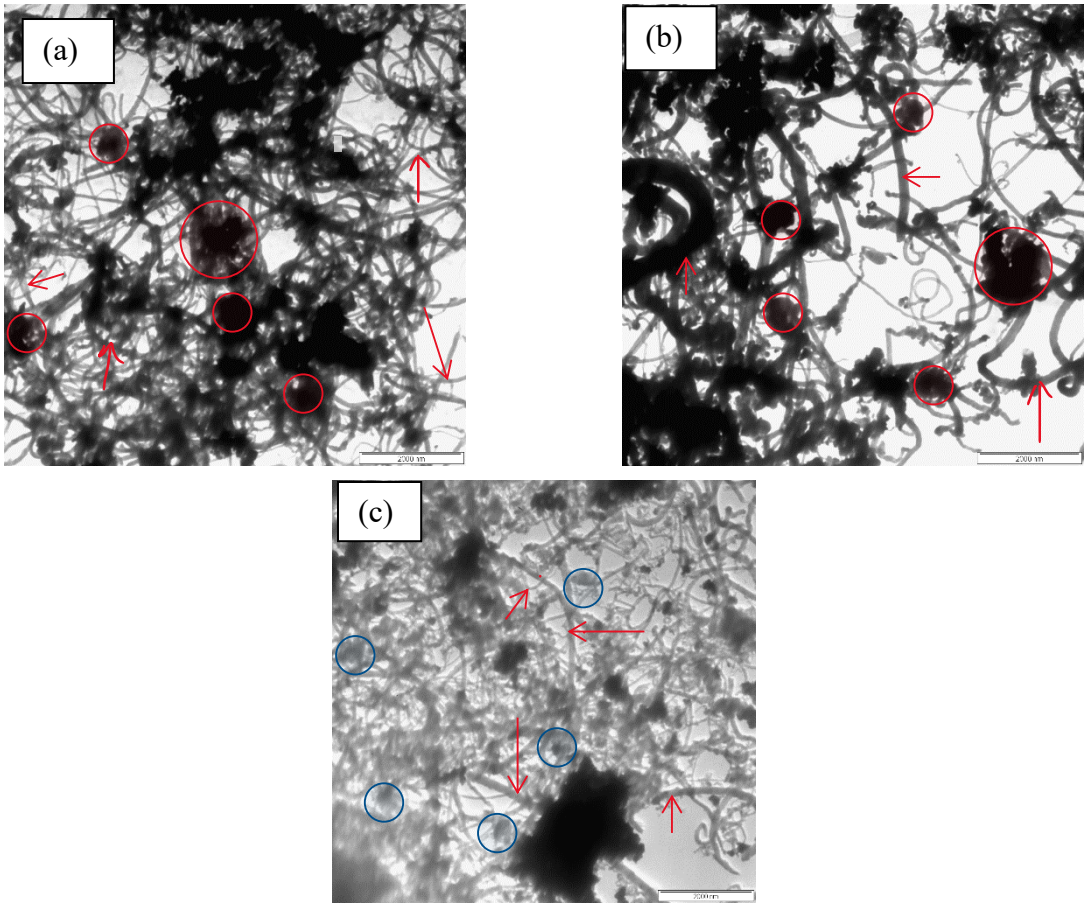

Fig. 12 TEM Images of the 20 wt.% Ni/Pr_2O_3 a) IWI b) US-WI c) PSG- 20 wt.% Ni/Pr_2O_3 at 15,000 × magnifications. (Scale bar for all images 2000 nm)

The quantitative study of the loss in weight (TG) and derivative weight loss (DTG) profiles of the 20 wt.% Ni/Pr_2O_3 spent catalysts (synthesized by the IWI, US-WI, and PSG methods) are depicted in Fig. 13 (a and b). The analyses were carried out at 25 - 900 ºC with ramping of 10 ºC min^{-1} in a 20% O_2/ 80% N_2 mixed-flow system. The weight loss shown in Fig. 13 a depicts that the TG profile represents carbon removal. The weight loss due to oxidation of carbon for the IWI, US-WI, and PSG catalysts were 47.22 %, 44.16 % and 18.04 %, respectively.

Also, the stability of the catalysts is dependent on the carbon species. The behavior of the samples in terms of their weight loss are linked to two types of carbonaceous species as confirmed by the TEM studies. According to previous studies, oxidation of easily oxidized filamentous or amorphous carbon occurs around 400 – 500 ºC, while above 500 ºC, the TG is attributed to encapsulated or graphitic carbon oxidation (Trimm 1999; Wang and Lu 2000; Koo et al. 2008).

DTG profile represented in Fig. 13b reveals two peaks for the IWI and US-WI catalysts respectively at point 1 and 2, while the DTG profile of the PSG catalysts also had two overlapping peaks at point 3 and 4. Peaks at point 1, visible in the range of 200 – 330 ºC for the spent IWI and US-WI catalysts represents the loss of adsorbed water.

Peaks at point 2 for the IWI and US-WI catalysts occurred in the range of 450 – 650 ºC and peaked at around 560 ºC. During the reaction study, for the IWI and US-WI catalysts, the reaction had stopped suddenly before 2 h of reaction time suggesting that catalyst deactivation had occurred. According to literature such reaction behavior can be as a result of graphitic or encapsulated carbon formation (Trimm 1999; Wang and Lu 2000; Koo

et al. 2008). Overlapping peaks at point 3 and 4 for the PSG catalyst occurred in the range of 400 – 650 °C. The initial peak at point 3 is significantly larger in size than the slightly visible peak at point 4. In relation to the behavior of the PSG catalyst during reaction (catalyst remained active after 2 h of reaction time) and to further explain the dual carbon types resulting from the double peaks, peak at point 3 (peaked at about 500°C) would likely be associated with the easily oxidized filamentous or amorphous carbon formation which corroborates with the FESEM analysis, whereas the less intense/visible peak at point 4 (peaked at around 600°C) is likely from the oxidation of graphitic carbon. The result shows that the PSG- 20wt% Ni/Pr_2O_3 catalyst has better resistance to deactivation amongst all prepared catalysts since dual carbon species are formed (filamentous and graphitic carbon) with a larger amount been filamentous carbon in nature. Moreover, the intensity of the peaks representing oxidation of carbon for the IWI and US-WI catalysts are much larger than the overlapping peaks representing the PSG catalyst. In addition, for the PSG catalyst, the intensity of the peak resulting from oxidation of filamentous carbon (peak at point 3) was larger than the peak representing the oxidation of graphitic carbon (peak at point 4), indicative of a higher amount of easily oxidized carbon than the unreactive carbon species in the spent PSG catalyst. In summary, the catalyst synthesized by the PSG method had greater stability as a result of the amount and type of carbon species formed.

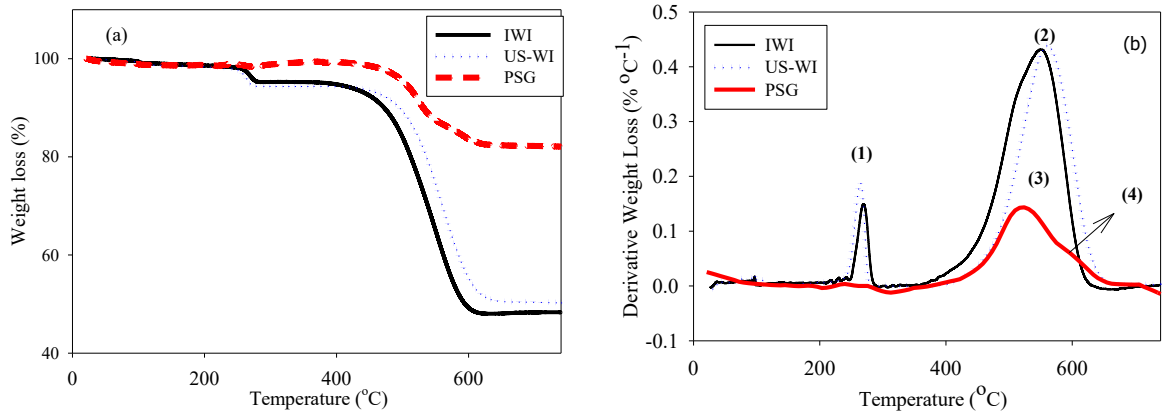

Fig. 13 TPO of the spent the 20 wt.% Ni/Pr_2O_3 catalysts a) weight loss b) derivative weight loss.

Conclusions

In the present study, three samples of 20 wt.% Ni/Pr_2O_3 were prepared by IWI, US-WI, and PSG methods. The variables investigated in the paper are the methods of preparation, catalysts' activity, reaction temperature and stability. The O 1s peaks confirmed a much better balance between lattice and adsorbed O_2 peaks for the PSG catalyst compared to the IWI and US-WI catalysts. The XPS result corroborated the results of the catalytic test carried out for all three samples after 2 h TOS at 800 ºC post-reduction. The catalytic test revealed that the average CH_4 conversions were approximately 88 % for the IWI, US-WI, and PSG synthesized catalysts, while average CO_2 conversions were 87.5%, 90% and 92%, for the IWI, US-WI, and PSG synthesized catalysts, respectively. However, before 2 h of the reaction time, the IWI and US-WI catalyzed reactions stopped because of total restriction of reactants' flow due to excessive carbon build-up. There was no significant different between the catalysts synthesized by IWI and US-WI methods as most of the experimental results and characterizations were

similar, hence the ultrasonication step for the US-WI catalysts did not significantly affect the 20 wt.% Ni/Pr_2O_3 catalyst in the MDR reaction.

The catalyst's crystallite size obtained using the Williamson-Hall equation was about 21.3 nm, 21.3 nm, and 10.6 nm, for IWI, US-WI, and PSG catalysts, respectively. This could further explain the reduction in carbon deposition and the catalyst stability in the reaction catalyzed by the PSG catalysts. Also, in the TGA profile, the amount of unreactive carbonaceous species was lower on the PSG catalysts because of reduced crystallite size, enhanced dispersion, and balance ratio in the oxygen species (lattice to adsorbed oxygen ratio).

During the temperature effects study (600 – 950 °C) at < 700 °C and > 900 °C for the PSG catalyst, side reactions like RWGS and Boudouard reaction significantly influenced the reaction outcomes. At 600 °C (lower temperature range), MDR reaction was affected by the WGS reaction, while at > 900 °C (higher temperature range) the net WGS reaction was negligible and the backward reaction i.e., the RWGS reaction dominated.

When compared to the IWI and US-WI synthesis methods, the PSG synthesis method offers better attraction because it allows for the preparation of catalysts with smaller crystallite size (10 nm) that are uniformly dispersed thereby enhancing the carbon gasification rate. Also, the relative ratio of oxygen species is closer to unity and higher (0.85) in the PSG catalyst as compared to the IWI (0.75) and US-WI (0.75) catalyst. As a result of this, the PSG catalyst attained stability in up to 24 h TOS because it accumulated more filamentous carbon, whereas the IWI and US-WI catalysts accumulated mainly graphitic carbon which encapsulated the Ni^0 active sites, causing excess carbon retention that clogged the reactor and restricted flow. However, the PSG catalysts could not withstand the rate of carbon deposition after 24 h which creates a platform for further studies on the possibility of enhancing the stability of the PSG- 20 wt. % Ni/ Pr_2O_3 catalysts by either using double support or promoters.

Acknowledgements

The authors extend their gratitude to Universiti Malaysia Pahang, Malaysia for the financial assistance through the International Publication Research Grant (RDU203304) and Post-Doctoral Fellowship for Osarieme Uyi Osazuwa.

References

Ahn K, Yoo DS, Prasad DH, et al (2012) Role of multivalent Pr in the formation and migration of oxygen vacancy in Pr-doped ceria: Experimental and first-principles investigations. Chem Mater 24:4261–4267. https://doi.org/10.1021/cm3022424

Ali ME, Rahman MM, Sarkar SM, Hamid SBA (2014) Heterogeneous metal catalysts for oxidation reactions. J Nanomater 2014:. https://doi.org/10.1155/2014/192038

Amin MH, Mantri K, Newnham J, et al (2012) Highly stable ytterbium promoted Ni/γ-Al2O3 catalysts for carbon dioxide reforming of methane. Appl Catal B Environ 119–120:217–226. https://doi.org/10.1016/j.apcatb.2012.02.039

Ay H, Üner D (2015) Dry reforming of methane over CeO2 supported Ni, Co and Ni–Co catalysts. Appl Catal B Environ 179:128–138. https://doi.org/10.1016/j.apcatb.2015.05.013

Ayodele B V., Abdullah SB, Cheng CK (2017) Kinetics and mechanistic studies of CO-rich hydrogen production by CH4/CO2reforming over Praseodymia supported cobalt catalysts. Int J Hydrogen Energy 42:28408–28424. https://doi.org/10.1016/j.ijhydene.2017.09.037

Ayodele B V., Hossain SS, Lam SS, et al (2016) Syngas production from CO2 reforming of methane over

neodymium sesquioxide supported cobalt catalyst. J Nat Gas Sci Eng 34:873–885. https://doi.org/10.1016/j.jngse.2016.07.059

Baharudin L, Rahmat N, Othman NH, et al (2022) Formation, control, and elimination of carbon on Ni-based catalyst during CO2 and CH4 conversion via dry reforming process: A review. J CO2 Util 61:102050. https://doi.org/10.1016/J.JCOU.2022.102050

Bai Y, Wang Y, Yuan W, et al (2019) Catalytic performance of perovskite-like oxide doped cerium (La 2 − x Ce x CoO 4 ± y) as catalysts for dry reforming of methane. Chinese J Chem Eng 27:379–385. https://doi.org/10.1016/j.cjche.2018.05.016

Ballesteros-Plata D, Infantes-Molina A, Rodríguez-Castellón E, et al (2022) Improving noble metal catalytic activity in the dry reforming of methane by adding niobium. Fuel 308:121996. https://doi.org/10.1016/J.FUEL.2021.121996

Baudouin D, Rodemerck U, Krumeich F, et al (2013) Particle size effect in the low temperature reforming of methane by carbon dioxide on silica-supported Ni nanoparticles. J Catal 297:27–34. https://doi.org/10.1016/j.jcat.2012.09.011

Botes FG, Niemantsverdriet JW, Van De Loosdrecht J (2013) A comparison of cobalt and iron based slurry phase Fischer-Tropsch synthesis. In: Catalysis Today. Elsevier, pp 112–120

Cao ANT, Pham CQ, Nguyen TM, et al (2022) Dysprosium promotion on Co/Al2O3 catalysts towards enhanced hydrogen generation from methane dry reforming. Fuel 324:124818. https://doi.org/10.1016/J.FUEL.2022.124818

Chen X, Yin L, Long K, et al (2020) The reconstruction of Ni particles on SBA-15 by thermal activation for dry reforming of methane with excellent resistant to carbon deposition. J Energy Inst 93:2255–2263. https://doi.org/10.1016/j.joei.2020.06.008

Danks AE, Hall SR, Schnepp Z (2016) The evolution of “sol-gel” chemistry as a technique for materials synthesis. Mater Horizons 3:91–112. https://doi.org/10.1039/c5mh00260e

de Caprariis B, de Filippis P, Palma V, et al (2016) Rh, Ru and Pt ternary perovskites type oxides BaZr(1-x)MexO3 for methane dry reforming. Appl Catal A Gen 517:47–55. https://doi.org/10.1016/J.APCATA.2016.02.029

Deraz NM (2018) The comparative jurisprudence of catalysts preparation methods: I. precipitation and impregnation methods. J Ind Environ Chem 2:19–21

Dimesso L (2018) Pechini processes: An alternate approach of the sol-gel method, preparation, properties, and applications. Handb Sol-Gel Sci Technol Process Charact Appl 1067–1087. https://doi.org/10.1007/978-3-319-32101-1_123

Ekeoma BC, Yusuf M, Johari K, Abdullah B (2022) Mesoporous silica supported Ni-based catalysts for methane dry reforming: A review of recent studies. Int J Hydrogen Energy. https://doi.org/10.1016/J.IJHYDENE.2022.05.297

Fan MS, Abdullah AZ, Bhatia S (2011) Hydrogen production from carbon dioxide reforming of methane over Ni-Co/MgO-ZrO2 catalyst: Process optimization. Int J Hydrogen Energy 36:4875–4886. https://doi.org/10.1016/j.ijhydene.2011.01.064

Fan MS, Abdullah AZ, Bhatia S (2009) Catalytic technology for carbon dioxide reforming of methane to synthesis gas. ChemCatChem 1:192–208. https://doi.org/10.1002/cctc.200900025

Fang X, Zhang J, Liu J, et al (2018) Methane dry reforming over Ni/Mg-Al-O: On the significant promotional

effects of rare earth Ce and Nd metal oxides. J CO2 Util 25:242–253. https://doi.org/10.1016/J.JCOU.2018.04.011

Franz R, Tichelaar FD, Uslamin EA, Pidko EA (2021) Dry reforming of methane to test passivation stability of Ni/ Al2O3 catalysts. Appl Catal A Gen 612:117987. https://doi.org/10.1016/J.APCATA.2021.117987

Gonçalves G, Lenzi MK, Santos OAA, Jorge LMM (2006) Preparation and characterization of nickel based catalysts on silica, alumina and titania obtained by sol-gel method. J Non Cryst Solids 352:3697–3704. https://doi.org/10.1016/j.jnoncrysol.2006.02.120

Gonzalez RD, Lopez T, Gomez R (1997) Sol-gel preparation of supported metal catalysts. Catal Today 35:293–317. https://doi.org/10.1016/S0920-5861(96)00162-9

Goula MA, Charisiou ND, Papageridis KN, Siakavelas G (2016) Influence of the synthesis method parameters used to prepare nickel-based catalysts on the catalytic performance for the glycerol steam reforming reaction. Cuihua Xuebao/Chinese J Catal. https://doi.org/10.1016/S1872-2067(16)62518-4

Han K, Yu W, Xu L, et al (2021) Reducing carbon deposition and enhancing reaction stability by ceria for methane dry reforming over Ni@SiO2@CeO2 catalyst. Fuel 291:120182. https://doi.org/10.1016/j.fuel.2021.120182

Himabindu B, Latha Devi NSMP, Rajini Kanth B (2021) Microstructural parameters from X-ray peak profile analysis by Williamson-Hall models; A review. Mater Today Proc 47:4891–4896. https://doi.org/10.1016/J.MATPR.2021.06.256

Jana P, De La Peña O'Shea VA, Coronado JM, Serrano DP (2010) Cobalt based catalysts prepared by Pechini method for CO2-free hydrogen production by methane decomposition. Int J Hydrogen Energy 35:10285–10294. https://doi.org/10.1016/j.ijhydene.2010.07.125

Jawad A, Rezaei F, Rownaghi AA (2020) Highly efficient Pt/Mo-Fe/Ni-based Al2O3-CeO2 catalysts for dry reforming of methane. Catal Today 350:80–90. https://doi.org/10.1016/j.cattod.2019.06.004

Jiang SP (2006) A review of wet impregnation - An alternative method for the fabrication of high performance and nano-structured electrodes of solid oxide fuel cells. Mater Sci Eng A 418:199–210. https://doi.org/10.1016/j.msea.2005.11.052

Kakihana M (1996) "Sol-Gel" preparation of high temperature superconducting oxides. J Sol-Gel Sci Technol 6:7–55. https://doi.org/10.1007/BF00402588

Khademi MH, Alipour-Dehkordi A, Tabesh M (2021) Optimal design of methane tri-reforming reactor to produce proper syngas for Fischer-Tropsch and methanol synthesis processes: A comparative analysis between different side-feeding strategies. Int J Hydrogen Energy 46:14441–14454. https://doi.org/10.1016/j.ijhydene.2021.01.215

Khajenoori M, Rezaei M, Meshkani F (2015) Dry reforming over CeO2-promoted Ni/MgO nano-catalyst: Effect of Ni loading and CH4/CO2 molar ratio. J Ind Eng Chem 21:717–722. https://doi.org/10.1016/J.JIEC.2014.03.043

Khalil M. (2003) Synthesis, X-ray, infrared spectra and electrical conductivity of La/Ba–CoO3 systems. Mater Sci Eng A 352:64–70. https://doi.org/10.1016/S0921-5093(02)00557-9

Khorsand Zak A, Abd. Majid WH, Abrishami ME, Yousefi R (2011) X-ray analysis of ZnO nanoparticles by Williamson–Hall and size–strain plot methods. Solid State Sci 13:251–256. https://doi.org/10.1016/j.solidstatesciences.2010.11.024

Kim DK, Stöwe K, Müller F, Maier WF (2007) Mechanistic study of the unusual catalytic properties of a new

Ni{single bond}Ce mixed oxide for the CO2 reforming of methane. J Catal 247:101–111. https://doi.org/10.1016/j.jcat.2007.01.011

Kim P, Kim Y, Kim H, et al (2004) Synthesis and characterization of mesoporous alumina for use as a catalyst support in the hydrodechlorination of 1,2-dichloropropane: effect of preparation condition of mesoporous alumina. J Mol Catal A Chem 219:87–95. https://doi.org/10.1016/J.MOLCATA.2004.04.038

Koo KY, Roh HS, Seo YT, et al (2008) Coke study on MgO-promoted Ni/Al2O3 catalyst in combined H2O and CO2 reforming of methane for gas to liquid (GTL) process. Appl Catal A Gen 340:183–190. https://doi.org/10.1016/j.apcata.2008.02.009

Kuhn JN, Ozkan US (2008) Surface properties of Sr- and Co-doped LaFeO3. J Catal 253:200–211. https://doi.org/10.1016/j.jcat.2007.10.005

Kwon BW, Oh JH, Kim GS, et al (2018) The novel perovskite-type Ni-doped Sr0.92Y0.08TiO3 as a reforming biogas (CH4 + CO2) for H2 production. Appl Energy 227:213–219. https://doi.org/10.1016/j.apenergy.2017.07.105

Kwon Y, Eichler JE, Mullins CB (2022) NiAl2O4 as a beneficial precursor for Ni/Al2O3 catalysts for the dry reforming of methane. J CO2 Util 63:102112. https://doi.org/10.1016/J.JCOU.2022.102112

Leclercq E, Rives A, Payen E, Hubaut R (1998) X-ray photoelectron spectroscopy and infrared spectroscopy studies for the mechanism of the enantioselective hydrogenation of methyl acetoacetate over mixed nickel-cerium oxides. Appl Catal A Gen 168:279–288. https://doi.org/10.1016/S0926-860X(97)00359-1

Lee G, Kim I, Yang I, et al (2018) Effects of the preparation method on the crystallinity and catalytic activity of LaAlO 3 perovskites for oxidative coupling of methane. Appl Surf Sci 429:55–61. https://doi.org/10.1016/j.apsusc.2017.08.092

Lee HC, Siew KW, Gimbun J, Cheng CK (2014) Synthesis and characterisation of cement clinker-supported nickel catalyst for glycerol dry reforming. Chem Eng J 255:245–256. https://doi.org/10.1016/j.cej.2014.06.044

Li B, Yuan X, Li L, et al (2021) Lanthanide oxide modified nickel supported on mesoporous silica catalysts for dry reforming of methane. Int J Hydrogen Energy 46:31608–31622. https://doi.org/10.1016/J.IJHYDENE.2021.07.056

Li H, Xu H, Wang J (2011) Methane reforming with CO2 to syngas over CeO 2-promoted Ni/Al2O3-ZrO2 catalysts prepared via a direct sol-gel process. J Nat Gas Chem 20:1–8. https://doi.org/10.1016/S1003-9953(10)60156-9

Li K, Pei C, Li X, et al (2020) Dry reforming of methane over La2O2CO3-modified Ni/Al2O3 catalysts with moderate metal support interaction. Appl Catal B Environ 264:118448. https://doi.org/10.1016/j.apcatb.2019.118448

Lin J, Yu M, Lin C, Liu X (2007) Multiform oxide optical materials via the versatile pechini-type sol-gel process: Synthesis and characteristics. J Phys Chem C 111:5835–5845. https://doi.org/10.1021/jp070062c

Liu D, Wang Y, Shi D, et al (2012) Methane reforming with carbon dioxide over a Ni/ZiO2-SiO 2 catalyst: Influence of pretreatment gas atmospheres. Int J Hydrogen Energy 37:10135–10144. https://doi.org/10.1016/j.ijhydene.2012.03.158

Lovell EC, Horlyck J, Scott J, Amal R (2017) Flame spray pyrolysis-designed silica/ceria-zirconia supports for the carbon dioxide reforming of methane. Appl Catal A Gen 546:47–57. https://doi.org/10.1016/j.apcata.2017.08.002

Luisetto I, Tuti S, Battocchio C, et al (2015) Ni/CeO2–Al2O3 catalysts for the dry reforming of methane: The effect of CeAlO3 content and nickel crystallite size on catalytic activity and coke resistance. Appl Catal A Gen 500:12–22. https://doi.org/10.1016/J.APCATA.2015.05.004

Luisetto I, Tuti S, Di Bartolomeo E (2012) Co and Ni supported on CeO2 as selective bimetallic catalyst for dry reforming of methane. Int J Hydrogen Energy 37:15992–15999. https://doi.org/10.1016/j.ijhydene.2012.08.006

Majid A, Tunney J, Argue S, et al (2005) Preparation of SrFeO∼2.85 perovskite using a citric acid assisted Pechini-type method. J Alloys Compd 398:48–54. https://doi.org/10.1016/j.jallcom.2005.02.023

Milberg B, Juan A, Irigoyen B (2017) Redox behavior of a low-doped Pr-CeO2(111) surface. A DFT+U study. Appl Surf Sci 401:206–217. https://doi.org/10.1016/J.APSUSC.2016.12.245

Mishra A, Shafiefarhood A, Dou J, Li F (2019) Rh promoted perovskites for exceptional "low temperature" methane conversion to syngas. Catal Today. https://doi.org/10.1016/j.cattod.2019.05.036

Moogi S, Hyun Ko C, Hoon Rhee G, et al (2022) Influence of catalyst synthesis methods on anti-coking strength of perovskites derived catalysts in biogas dry reforming for syngas production. Chem Eng J 437:135348. https://doi.org/10.1016/J.CEJ.2022.135348

Mora-Barrantes I, Rodríguez A, Ibarra L, et al (2011) Overcoming the disadvantages of fumed silica as filler in elastomer composites. J Mater Chem 21:7381–7392. https://doi.org/10.1039/c1jm10410a

Moradi GR, Rahmanzadeh M, Khosravian F (2014) The effects of partial substitution of Ni by Zn in LaNiO3 perovskite catalyst for methane dry reforming. J CO2 Util 6:7–11. https://doi.org/10.1016/j.jcou.2014.02.001

Mustu H, Yasyerli S, Yasyerli N, et al (2015) Effect of synthesis route of mesoporous zirconia based Ni catalysts on coke minimization in conversion of biogas to synthesis gas. Int J Hydrogen Energy 40:3217–3228. https://doi.org/10.1016/j.ijhydene.2015.01.023

Nabgan W, Mat R, Abdullah TAT, et al (2016) Development of a kinetic model for hydrogen production from phenol over Ni-Co/ZrO2 catalyst. J Environ Chem Eng 4:4444–4452. https://doi.org/10.1016/j.jece.2016.10.013

Odedairo T, Chen J, Zhu Z (2013) Metal-support interface of a novel Ni-CeO2 catalyst for dry reforming of methane. Catal Commun 31:25–31. https://doi.org/10.1016/j.catcom.2012.11.008

Osazuwa OU, Abidin SZ (2020) An overview on the role of lanthanide series (rare earth metals) in H2 and syngas production from CH4 reforming processes. Chem Eng Sci 227:115863. https://doi.org/10.1016/j.ces.2020.115863

Osazuwa OU, Abidin SZ, Fan X, et al (2021) An insight into the effects of synthesis methods on catalysts properties for methane reforming. J Environ Chem Eng 9:105052. https://doi.org/10.1016/j.jece.2021.105052

Osazuwa OU, Setiabudi HD, Rasid RA, Cheng CK (2017) Syngas production via methane dry reforming: A novel application of SmCoO3 perovskite catalyst. J Nat Gas Sci Eng 37:435–448. https://doi.org/10.1016/j.jngse.2016.11.060

Owgi AHK, Jalil AA, Hussain I, et al (2022) Enhancing resistance of carbon deposition and reaction stability over nickel loaded fibrous silica-alumina (Ni/FSA) for dry reforming of methane. Int J Hydrogen Energy. https://doi.org/10.1016/J.IJHYDENE.2021.12.134

Passos FB, de Oliveira ER, Mattos L V., Noronha FB (2005) Partial oxidation of methane to synthesis gas on

Pt/CexZr1−xO2 catalysts: the effect of the support reducibility and of the metal dispersion on the stability of the catalysts. Catal Today 101:23–30. https://doi.org/10.1016/J.CATTOD.2004.12.006

Pechini MP, Pechini M, Pechini M, Pechini MP (1967) Method of Preparing Lead and Alkaline Earth Titanates and Niobates and Coating Method Using the Same to Form a Capacitor 1967

Pizzolitto C, Pupulin E, Menegazzo F, et al (2019) Nickel based catalysts for methane dry reforming: Effect of supports on catalytic activity and stability. Int J Hydrogen Energy 44:28065–28076. https://doi.org/10.1016/J.IJHYDENE.2019.09.050

Rezaei M, Alavi SM, Sahebdelfar S, Yan ZF (2006) Syngas Production by Methane Reforming with Carbon Dioxide on Noble Metal Catalysts. J Nat Gas Chem 15:327–334. https://doi.org/10.1016/S1003-9953(07)60014-0

Roslan NA, Zainal Abidin S, Osazuwa OU, et al (2022) Enhanced syngas production from glycerol dry reforming over Ru promoted -Ni catalyst supported on extracted Al2O3. Fuel 314:123050. https://doi.org/10.1016/J.FUEL.2021.123050

Sajjadi SM, Haghighi M, Rahmani F (2015) Sol-gel synthesis of Ni-Co/Al2O3-MgO-ZrO2 nanocatalyst used in hydrogen production via reforming of CH4/CO2 greenhouse gases. J Nat Gas Sci Eng 22:9–21. https://doi.org/10.1016/j.jngse.2014.11.014

Schwengber CA, Da Silva FA, Schaffner RA, et al (2016) Methane dry reforming using Ni/Al2O3 catalysts: Evaluation of the effects of temperature, space velocity and reaction time. J Environ Chem Eng 4:3688–3695. https://doi.org/10.1016/J.JECE.2016.07.001

Sepehri S, Rezaei M, Wang Y, et al (2018) The evaluation of autothermal methane reforming for hydrogen production over Ni/CeO2 catalysts. Int J Hydrogen Energy 43:22340–22346. https://doi.org/10.1016/J.IJHYDENE.2018.10.016

Setiabudi HD, Chong CC, Abed SM, et al (2018) Comparative study of Ni-Ce loading method: Beneficial effect of ultrasonic-assisted impregnation method in CO2 reforming of CH4 over Ni-Ce/SBA-15. J Environ Chem Eng 6:745–753. https://doi.org/10.1016/j.jece.2018.01.001

Shin SA, Noh YS, Hong GH, et al (2018) Dry reforming of methane over Ni/ZrO2-Al2O3 catalysts: Effect of preparation methods. J Taiwan Inst Chem Eng 90:25–32. https://doi.org/10.1016/j.jtice.2017.11.032

Singh S, Bahari MB, Abdullah B, et al (2018) Bi-reforming of methane on Ni/SBA-15 catalyst for syngas production: Influence of feed composition. Int J Hydrogen Energy 43:17230–17243. https://doi.org/10.1016/j.ijhydene.2018.07.136

Son IH, Lee SJ, Song IY, et al (2014) Study on coke formation over Ni/γ-Al2O3, Co-Ni/γ-Al2O3, and Mg-Co-Ni/γ-Al2O3 catalysts for carbon dioxide reforming of methane. Fuel 136:194–200. https://doi.org/10.1016/j.fuel.2014.07.041

Song Z, Liu W, Nishiguchi H, et al (2007) The Pr promotion effect on oxygen storage capacity of Ce-Pr oxides studied using a TAP reactor. Appl Catal A Gen 329:86–92. https://doi.org/10.1016/j.apcata.2007.06.023

Sun Z, Liu H, Bai H, et al (2022) The crucial role of deoxygenation in syngas refinement and carbon dioxide utilization during chemical looping-based biomass gasification. Chem Eng J 428:132068. https://doi.org/10.1016/J.CEJ.2021.132068

Trimm D. (1999) Catalysts for the control of coking during steam reforming. Catal Today 49:3–10. https://doi.org/10.1016/S0920-5861(98)00401-5

Trueba M, Trasatti SP (2005) γ-alumina as a support for catalysts: A review of fundamental aspects. Eur J Inorg

Chem 3393–3403. https://doi.org/10.1002/ejic.200500348

Varkolu M, Kunamalla A, Jinnala SAK, et al (2021) Role of CeO2/ZrO2 mole ratio and nickel loading for steam reforming of n-butanol using Ni–CeO2–ZrO2–SiO2 composite catalysts: A reaction mechanism. Int J Hydrogen Energy 46:7320–7335. https://doi.org/10.1016/j.ijhydene.2020.11.240

Wang S, Lu GQ (Max), Millar GJ (1996) Carbon Dioxide Reforming of Methane To Produce Synthesis Gas over Metal-Supported Catalysts: State of the Art. Energy & Fuels 10:896–904. https://doi.org/10.1021/ef950227t

Wang S, Lu GQM (2000) Effects of promoters on catalytic activity and carbon deposition of Ni/g -Al2O3 catalysts in CO2 reforming of CH4. J Chem Technol Biotechnol 595:589–595. https://doi.org/10.1002/1097-4660(200007)75:7<589::AID-JCTB241>3.0.CO;2-7

Whang HS, Choi MS, Lim J, et al (2017) Enhanced activity and durability of Ru catalyst dispersed on zirconia for dry reforming of methane. Catal Today 293–294:122–128. https://doi.org/10.1016/j.cattod.2016.12.034

Yosefi L, Haghighi M, Allahyari S, Ashkriz S (2015) Effect of ultrasound irradiation and Ni-loading on properties and performance of CeO2-doped Ni/clinoptilolite nanocatalyst used in polluted air treatment. Process Saf Environ Prot 95:26–37. https://doi.org/10.1016/j.psep.2015.02.006

Zanganeh R, Rezaei M, Zamaniyan A (2013) Dry reforming of methane to synthesis gas on NiO-MgO nanocrystalline solid solution catalysts. Int J Hydrogen Energy 38:3012–3018. https://doi.org/10.1016/j.ijhydene.2012.12.089

Zhang G, Du Y, Xu Y, Zhang Y (2014) Journal of Industrial and Engineering Chemistry Effects of preparation methods on the properties of cobalt / carbon catalyst for methane reforming with carbon dioxide to syngas. J Ind Eng Chem 20:1677–1683. https://doi.org/10.1016/j.jiec.2013.08.016